Morphology and thermodynamics of polymers with monofunctional hydrogen bonding ends in dilute and semidilute concentration

Eunsang Lee* and Wolfgang Paul
Institute for Physics, Martin-Luther University Halle-Wittenberg, Halle 06120, Germany

(Received 18 April 2019; published 8 July 2019)

Rheological properties of supramolecular polymers (SMPs) depend on their equilibrium structure including the size, the number, and the topology of aggregates. A polymer with a hydrogen bonding (H-bonding) motif at both ends is one widely used precursor to build SMPs. Due to the complex interplay between chain stiffness, H-bonding interaction, polarity along a chain, and polymer conformational entropy, it is difficult to theoretically predict the structure of SMPs. In this work we investigate thermodynamics of SMPs with H-bonding ends in a wide range of densities. A replica exchange stochastic approximation Monte Carlo method with coarse-grained models for polyethylene and polybuthylene glycols is used. Our simulation shows that SMPs have two morphological transition lines with increasing temperature, a ring-linear transition, and a linear-free chain transition. The latter is a thermodynamic transition and turns out to be continuous. Comparing the two different spacers, we find that ring-linear transition temperatures differ from each other at the constant volume fraction due to different looping probabilities, which can be calculated from the average polymer size by mean field. However, the linear-free chain transition temperatures are similar because the entropic penalty to form a hydrogen bond mainly depends on the probability of finding H-bonding groups in a system, which is the same for both systems at a given volume fraction.

DOI: 10.1103/PhysRevE.100.012502

I. INTRODUCTION

Polymers functionalized by associating groups which are able to make a noncovalent bond have a transient morphology which varies depending on external stimuli, e.g., temperature and shear stress [1–6]. The material made by such associating polymers is usually called supramolecular polymer (SMP), and it shows characteristic rheological properties including shear thinning and thickening, as well as novel smart functions like self-healing [7,8].

One widely used motif to achieve the physical association is the hydrogen bond (H bond) [9–18], due to its association strength and directionality. Especially, its binding strength is relatively weak compared to the covalent one, which makes it reversible at room temperature by thermal fluctuations. Due to such reversible bonds, the equilibrium morphology of SMPs can be thermodynamically controlled and its resulting rheology can also be manipulated. Together with the H-bonding moiety, hydrophilicity of the associating group (a sticker), backbone (a spacer), and solvent play an important role to determine the mesoscopic structure. Interesting morphologies affecting a material's rheology like a flowerlike micelle [19,20], a film [21], a fibril [15,22], or a gel [19,23] have been experimentally observed.

Another interesting suggestion about SMP morphologies in recent studies was the presence of a ring-shaped aggregate. Bras *et al.* have recently synthesized a poly(ethylene glycol) (PEG) functionalized at both ends by ureidopyrimidinone (UPY) and have found an evidence for the formation of ring aggregates using a small-angle neutron-scattering experiment [24]. From a physical point of view, two conditions are necessary for the pure H-bond-based ring formation: The first is that both spacer and sticker are hydrophilic to prevent phase segregation. The second is that the sticker should be monofunctional, and it form an H bond with only one other sticker. The above experiment done with PEG spacers and UPY stickers [13,14] fulfills both conditions. Because a formed ring aggregate has no chain end to aggregate with another precursor, the average molecular weight of aggregates tends to decrease resulting in fast diffusion of the molecule. On the other hand, even if the ring aggregates are not permanent, relaxation of the resulting material becomes slow by topological effects of the ring such as ring-linear threading [25–27], knotting [28], and concatenation of rings which have been studied for inherent ring polymer systems (or ring-linear blends). However, there is still a lack of complete understanding for the ring effect on SMPs, and it is highly challenging to analyze experimental results dealing with different polymer topologies from a microscopic point of view.

To overcome the difficulty, theoretical [29–32] and numerical studies [33–38] have been done for SMP structure and dynamics. Equilibrium statistics of bifunctional monomers by linear polycondensation has been investigated using classical polymerization theory [29–32] and the concept of living polymers [33–35] to estimate the fraction of microscopic rings and their size. However, those works have focused only on the bifunctional association but have not considered an effect of polymer conformations and sticker properties. Recently, researchers have studied the behavior of associating polymers using molecular dynamics [39–41] and Monte Carlo simulations [42–44]. Most of them employed a nondirectional

*eunsang.lee@physik.uni-halle.de

association potential between stickers such as the Lennard-Jone potential, which allows branched H bonds. Such systems are known to form a transient gel whose rheology is completely different from that of ring-shaped SMPs. More recent works done by Dormidontova *et al.* have used a directionally specific H-bond potential and investigated the equilibrium statistics of SMPs focusing on the rings [36–38]. They found a ring-linear transition at a certain density, but a complete picture of SMP thermodynamics in volume fraction–temperature (ϕ-T) space is still poorly developed, which will be addressed in this study.

Regarding the thermodynamics of SMP systems, we have investigated a single-molecule SMP precursor with H-bonding motifs assuming a dilute concentration regime and have found that the relative stability of a ring aggregate compared to a linear one nonmonotonically varies as a function of degree of polymerization [45]. It was also observed that the ring-linear transition shows phase coexistence regardless of the order of the transition. In this work, we move our focus to the SMPs in dilute and semidilute concentrations. We also study the behavior of different spacer systems, PEG and poly(butylene glycol) (PBG). We use replica exchange stochastic approximation Monte Carlo (RESAMC) simulation to sample a huge configurational space and construct densities of states (DOS). From the obtained DOS, canonical properties are calculated to understand the phase behavior and the transitions involved in a wide range of density and temperature.

This paper is organized as follows. The next section explains the model and the method we used. Under Results and Discussion, we explain how to obtain canonical properties from a DOS and how to define morphologies as well as the transition temperatures between them. The order of the transition will be also discussed. Using the obtained transition temperatures, we draw a ϕ-T phase diagram for both PEG and PBG spacer systems and discuss it. Finally, a conclusion section follows at the end of the paper.

II. MODEL AND COMPUTATIONAL METHODS

Each system in this study includes only one type of SMP precursor, which is a so-called self-complementary SMP. The precursor is composed of a polymer backbone with two H-bonding groups at the ends. Earlier, we developed a coarse-grained model for the SMP precursors mimicking PEG and PBG based on their atomistic structure generated from an all-atom force field [45]. In this model, one monomeric unit of PEG and PBG is coarse-grained to one spherical bead. Bonded interactions are composed of bond angle, bond length, and dihedral angle potentials, determined by Boltzmann inversion from the distributions obtained for these internal degrees of freedom from atomistic simulations. One difference between coarse-grained PEG and PBG is the chain stiffness, in that the persistence length of PEG is smaller than of PBG. Also, a PBG chain has larger spatial size than a PEG chain of the same degree of polymerization. Due to the hydrophilic characteristic of H-bonding stickers as well as monomers, we can coarse-grain the SMP model disregarding the possibility of phase segregation. The nonbonded interaction thus only consists of a repulsive Lennard-Jones potential. Even if solvent particles are not explicitly included in this model, this choice represents our polymers in a good solvent condition. For simplicity, an H-bonding sticker is also parameterized by a bead whose bonded and nonbonded interaction parameters are the same as the PEG bead. Additionally, a phenomenological nonbonded interaction potential is employed to describe the directional H-bonding interactions between sticker beads, with functional form given by [46]:

$$U_{\rm hb}(r_{ij},\vec{i}_k,\vec{j}_l) = -\epsilon_{\rm hb}G(r_{ij};R_{\rm hb},\sigma_R) \times G(\vec{i}_k\hat{r}_{ij};1,\sigma_\theta)G(\vec{i}_l\hat{r}_{ij};-1,\sigma_\theta), \quad (1)$$

where $G(x;\bar{m},\sigma)$ is a Gaussian function with mean $\bar{m}$ and standard deviation σ. r_{ij} and $\vec{i}_k$ are the distance between two stickers and the unit vector from a sticker-connected polymer bead to the ith sticker bead. $\epsilon_{\rm hb}$ and $R_{\rm hb}$ are energy gain and mean distance between two stickers on forming a hydrogen bond, respectively. σ_R and σ_θ represent standard deviations for the distance between stickers and the angles between backbone bonds leading to the stickers. In this equation, the last two Gaussian functions provide the angle specificity of the H bond. More details of the H-bonding potential can be found in our previous work [45] and the original work implementing Eq. (1) [46]. Parameters are determined based on the chemical structure of two H-bonded stickers. One advantage of this potential function is that we can tune the strength and the functionality of the H bond to change association nature. In the ground state of the UPY-UPY interaction, four chemical H bonds are formed. Because the typical H-bond strength in the gas phase is 15–20 kJ/mol [47], we set $\epsilon_{\rm hb} = 60$ kJ/mol, which is also consistent with the recent finding from SMP systems [17,18]. From a rough estimation of the distance between two sticker beads at the typical H-bond distance, we set $R_{\rm hb} = 0.5$ nm and $\sigma_R = 0.1$. Functionality of the sticker association depends intricately on the chemical structure of the sticker. Because the UPY sticker in dilute concentration is known to be monofunctional due to its bulky size [24], σ_θ has to be carefully determined to secure this monofunctionality. To do so, we calculate the ground-state energy and its configuration when three or four sticker groups, each of which is composed of connected PEG-UPY beads, come together. We use stochastic approximation Monte Carlo for this calculation, which will be discussed shortly.

Figure 1 shows the maximum value of the H-bonding energy gain when three and four sticker groups come together in space as a function of σ_θ. Representative snapshots for $\sigma_\theta = 0.1$ and 0.5 are also presented. With a large value of σ_θ, a wide range of angles of two adjacent sticker groups is allowed, resulting in multifunctional association and a branching structure. However, as σ_θ decreases to 0.1, only one-to-one H bonding is allowed, and the branching structure is excluded. Therefore, we set $\sigma_\theta = 0.1$ to guarantee the monofunctionality of the sticker.

Using the H-bond parameters described above, we performed simulations for SMP systems. We compared the difference between SMPs composed of PEG and PBG spacers. For all SMPs, the number of beads, N, is 8, including sticker beads at the ends. With a fixed simulation box size $L =$ 6 nm for PEG and $L = 9$ nm for PBG, different numbers of polymers M are included from $M = 2$ to 128, which corresponds to volume fractions of the coarse-grained beads

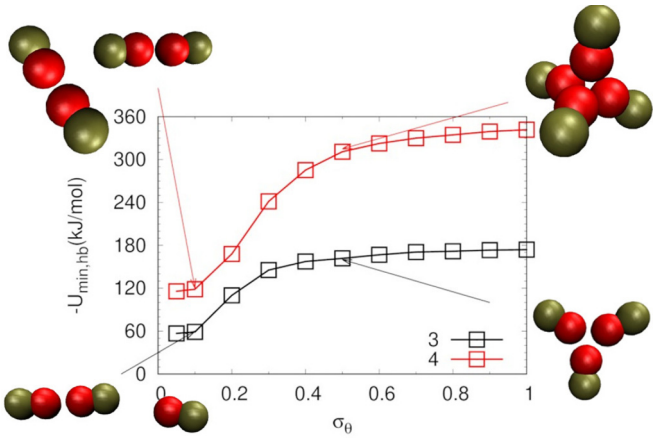

FIG. 1. Ground-state energies of H-bonding groups and their corresponding conformations as a function of σ_θ. Black and red (gray) lines indicate the H-bonding energy gain from three and four sticker groups coming together in space, respectively. Representative snapshots at $\sigma_\theta = 0.1$ (left) and 0.5 (right) are also shown. In the snapshots, red and cyan beads represent sticker and spacer beads, respectively.

from $\phi = 0.008$ to 0.521 for PEG and from 0.003 to 0.203 for PBG. From molecular dynamics simulations at $T = 300$ K with our coarse-grained models, we obtained that the end-to-end distance at dilute concentration is $R = 1.64$ nm for PEG and 2.44 nm for PBG, leading to overlap concentrations $\phi^* = N\sigma^3/R^3 = 0.20$ for PEG and 0.079 for PBG. So our simulation densities cover the dilute to semidilute regimes.

In this study, a RESAMC is used to sample the configuration randomly traveling across the energy space. The SAMC method is a flat histogram Monte Carlo method which constructs the density of energy states [48–52]. The obtained DOS can be transformed into any ensemble properties, e.g., of the canonical ensemble. Using this scheme, we obtain exact thermodynamic properties even very close to transition points. However, in order to get a converged DOS, it is necessary to visit all energies of interest equally which takes prohibitively long time for a large system. It should be noted that by the normal flat histogram method without any bias, the probability of finding a lowest-energy configuration is $\exp(10^3) \approx 10^{434}$ times lower than that of a high-energy configuration even if the microcanonical entropy difference between two energies is only $10^3 k_B$, where k_B is Boltzmann constant.

A few methods using multiple computing cores have been proposed to overcome the resource problem, one of which is replica exchange Wang-Landau (REWL) sampling [53,54]. The basic concept of the REWL is analogous to the conventional replica exchange canonical simulation [55], but instead of sampling conformations at different temperatures, several independent random walkers travel in the different energy windows. Adjacent windows have overlapping energies and the configurations are exchanged in every few steps of the Wang-Landau simulation with the following probability:

$$P_{\rm acc}(i \leftrightarrow j) = \min\left[1, \frac{g_i(U(X))}{g_i(U(Y))}\frac{g_j(U(Y))}{g_j(U(X))}\right], \qquad (2)$$

where $g_i[U(X)]$ means the DOS of the configurational energy U of configuration X in the ith energy window. We apply this method to the SAMC scheme, which is called RESAMC. The configuration exchange is tried every 10^3 MC steps (MCS) and the total simulation time is at least 10^8 MCS. The number of windows is 4–28 depending on the system size. After getting converged DOSs in all energy windows, a complete DOS is obtained by joining DOSs for which the difference between $\mathrm{d}\ln g(U)/\mathrm{d}U$ of adjacent windows is smallest. The bin size of energy in all energy windows is 1 kJ except for large systems of $M = 64$ and 128 which have a 2-kJ-wide energy bin.

Using the DOS in configurational energy space obtained by RESAMC, we construct the DOS as a function of total energy $g(E)$ by using a convolution of $g(U)$ and the DOS for the kinetic energy, $g(K)$ [56]. Here $g(K)$ is proportional to the area of a d-dimensional hypersphere of a radius K, where $d = 3N_{\rm tot}$ is the number of degrees of freedom for the kinetic energy, $N_{\rm tot}$ is the number of particles in a system, leading to $g(K) = \kappa K^{3N_{\rm tot}/2-1}$ where κ is a prefactor for $g(K)$. The relation for $g(E)$ is therefore

$$g(E) = \kappa \sum_{U=U_{\rm min}}^{U_{\rm max}} \int_0^\infty dK\, g(U) K^{3N_{\rm tot}/2-1} \delta(E-K-U). \quad (3)$$

In this equation, $U_{\rm min}$ and $U_{\rm max}$ denote the minimum and the maximum values of configurational energy in the RESAMC sampling and δ is a Dirac delta function.

III. RESULTS AND DISCUSSIONS

We first show how we construct the DOS as a function of total energy by RESAMC with an example of a $N = 8$, $M = 16$ PEG system in Fig. 2. All figures afterward are for the PEG system of $N = 8$, $M = 16$, and $L = 6.0$ nm if no additional information is given in the caption. One can see that every random walker makes a round trip from highest- to lowest-energy windows in roughly 1.5×10^6 MCS Fig. S1 in the Supplementary Material [57]. We perform the simulation for 10^8 MCS which we believe to be long enough for all walkers to sufficiently travel across all energy windows. As shown in Fig. 2, all pieces of DOSs join to make a complete DOS in a wide range of energy. The difference between DOSs

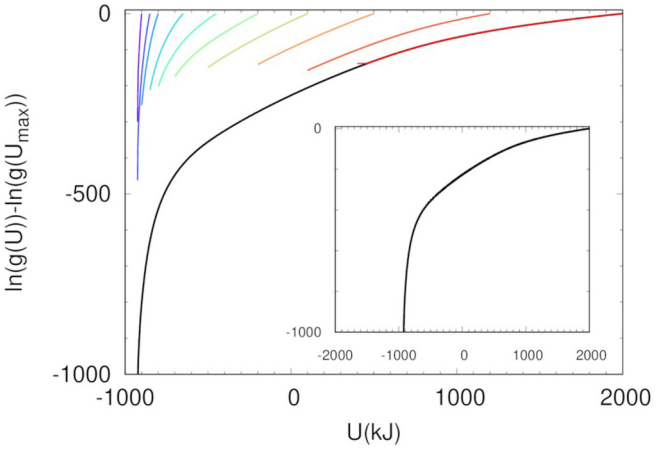

FIG. 2. The combined DOS as well as DOSs in each energy window for a $M = 16$ PEG system.

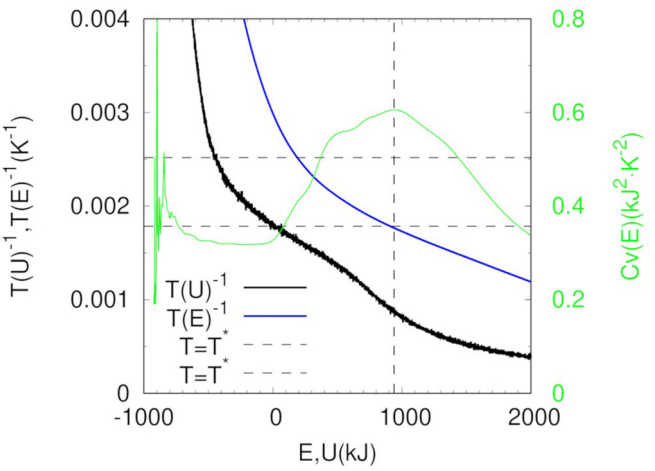

FIG. 3. Microcanonical inverse temperature as a function of total (blue, gray) and configurational energies (black) and the microcanonical specific heat obtained from the derivative of the inverse temperature with respect to total energy (green, light gray) for the $M = 16$ PEG system. The dashed lines indicate the position of the maximum of $C_v(E)$ and the corresponding inverse temperature.

of lowest and highest energies turns out to be more than e^{1000} for this system, which indicates a huge configurational space to be sampled within a single energy window.

From the obtained DOS as a function of U in Fig. 2 we obtain the DOS as a function of E, $g(E)$, using Eq. (3). Figure 3 shows the inverse microcanonical temperatures as a function of E and U, calculated by $T^{-1}(U) = k_B \partial \ln g(U)/\partial U$ and $T^{-1}(E) = k_B \partial \ln g(E)/\partial E$. Since the DOS for the energy E is summed over all $g(U)$ for possible U smaller than E multiplied by the DOS of the kinetic energy, $E - U$, $T^{-1}(E)$ is smoother than $T^{-1}(U)$. We calculate the microcanonical specific heat using the relation $C_v(E) = -T^{-2}\partial^2 \ln g(E)/\partial^2 E$ shown by a green line in Fig. 3. The maximum of $C_v(E)$ is located at $E = 939$ kJ which corresponds to $T = 560$ K from $T^{-1}(E)$, and the configurational energy at this temperature is $U \approx 100$ kJ from $T^{-1}(U)$. Although it is not clearly distinguished, a small shoulder peak exists around $E \approx 190$ kJ, corresponding to $T \approx 400$ K and $U \approx -450$ kJ. Noisy peaks near the ground-state energy are believed to originate from poor convergence in this energy regime.

Representative simulation snapshots for different configurational energies provide an evidence of the nature of the transitions in Fig. 3. Figure 4(a) shows the very low energy configuration involving ring-shaped aggregates. Because the lowest configurational energy is achieved from the complete formation of H bonds, a free chain end does not exist. $g(U)$ of this very low energy configuration is extremely low because of the looping conformation. Therefore, a ring aggregate is energetically favorable but entropically unfavorable and dominates at low temperature. A very high energy configuration, whose snapshot is not drawn in this figure, contains free polymers without any H bonds. Such a vaporized polymer configuration is entropically favorable, so it dominates at high temperature. In between, the configuration of $U = -300$ kJ in Fig. 4(b) involves linear-shaped aggregates which emerge in the middle temperature range.

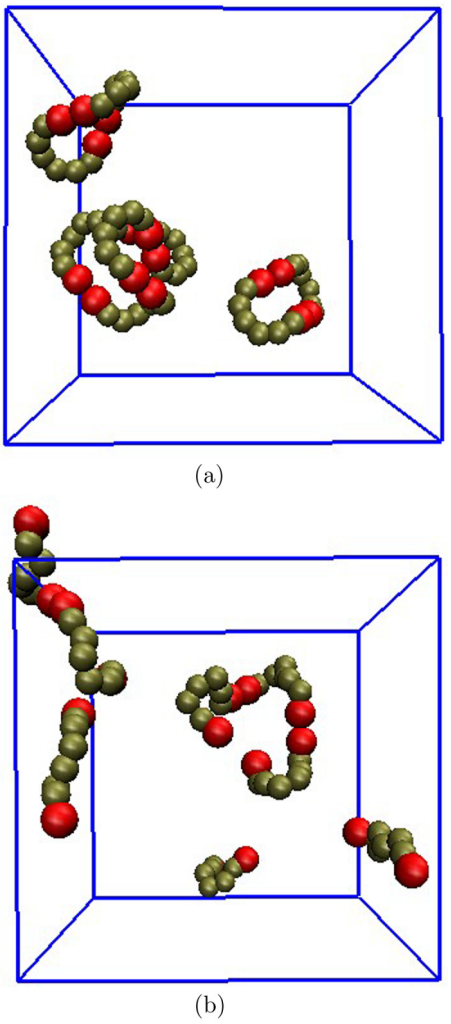

FIG. 4. Representative snapshots of a $M = 16$ PEG system for (a) low energy, $U = -800$ kJ, and (b) intermediate energy, $U = -300$ kJ. Some molecules are not shown for clarity.

It is possible to identify the transitions between different morphologies using the number of H bonds as a function of U. Figure 5 shows the ratio of the number of H bonds to the maximum possible number of H bonds which is M in a system. For example, the system of $M = 16$ contains $2M = 32$ stickers, which can make at most $M = 16$ H bonds. In this work, we define that an H bond is formed if its potential energy in Eq. (1) is smaller than -1 kJ. Even if this criterion can later lead to a slight shift of the transition temperature, such a fixed value of energy gain to define an H bond is necessary because configurations are sampled in energy space. The effect of this choice will be discussed shortly. The number of H bonds plotted by a black line in Fig. 5 decreases with increasing energy. The steepest slope of the decrease is at $U \approx 100$ kJ, which is consistent with the position of the maximum $C_v(E)$ in Fig. 3. This specifically indicates the transition at $E = 939$ kJ (or $T = 560$ K) below which the linear aggregates dominate and above which any H bond is not formed. We define this transition as linear-free chain transition, which is similar to a condensation-evaporation transition. Observing the number of H bonds participating in the formation of

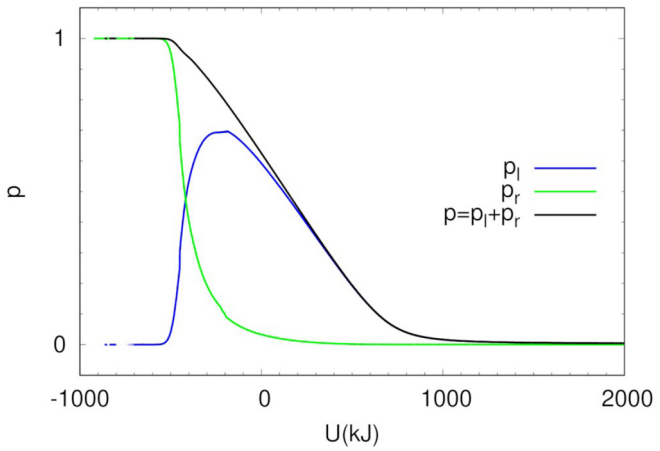

FIG. 5. The ratio of the number of H bonds to the maximum possible number of H bonds for a $M = 16$ PEG system. Blue (gray), green (light gray), and black lines indicate the ratio of H bonds in linear aggregates, ring aggregates, and the sum of these two, respectively.

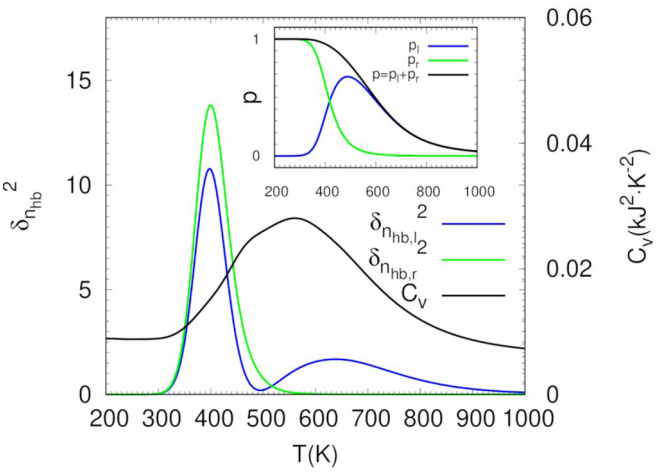

FIG. 6. The fluctuations of the number of H-bonds in linear (blue, gray) and ring aggregates (green, light gray) as a function of T together with the specific heat (black) on the right axis for a $M = 16$ PEG system. The inset shows the fraction of H-bonded stickers out of the number of stickers in the system, the fractions of bonded stickers contributing to the formation of ring aggregates (green, light gray) and of the linear aggregates (blue, gray).

ring and linear aggregates separately (blue and green lines in Fig. 5, respectively), we can find another morphological transition at $U \approx -450$ kJ. At this energy, H-bond fractions in ring and linear aggregates cross each other pointing out the conversion between ring and linear aggregates. This configurational energy is also consistent with the values observed from the shoulder peak in Fig. 3, $T \approx 400$ K and $E \approx 190$ kJ. Here we can also see that the formation of H-bonds in linear aggregates mostly contributes to the change of a total H-bonds decrease at $U \approx 100$ kJ.

Canonical averages of observables obtained from $g(E)$ by Laplace transformation are sometimes more useful to compare the simulation data with experimental data. We calculate various canonical functions by using the relation $\langle O(T)\rangle = \sum_E \bar{O}(E) g(E) \exp(-\beta E)/Z(T)$, where $\bar{O}(E)$ is a microcanonical average of an observable, β is inverse temperature, and $Z(T)$ is the canonical partition function calculated by $Z(T) = \sum_E g(E) \exp(-\beta E)$. We first show the canonical specific heat $C_v(T) = (\langle E^2\rangle - \langle E\rangle^2)/T^2$ in Figs. 6 and S2. We also plot $C_v(T)$ constructed from $g(U)$ in Fig. S2 of the Supplemental Material [57]. The two functions have almost the same shape but different heights due to the contribution of the kinetic energy. One can also find that the positions of the maxima are almost the same, $T^* = 558$ K from U and 560 K from E. This small deviation comes from the finite configuration energy range used in integration of Eq. (3). T^* in $C_v(T)$ also agrees with the microcanonical transition temperature in Fig. 3. A shoulder peak at $T \approx 400$ K is also weakly seen as in the microcanonical specific heat.

We also calculate the number of H bonds and its fluctuation as a function of temperature shown in Fig. 6. As explained, the system undergoes a transition corresponding to the H-bond breaking-forming event at the temperature of the maximum in $C_v(T)$. The position of this transition is from now on denoted as $T^* = T_l^*$. Comparing $C_v(T)$ and the fluctuation of H bonds, the transition at $T = T_l^*$ is due mostly to H bonds of linear aggregates shown by a blue line. Again, a little difference between the peak positions of these two is observed, which is caused by the criterion of definition for H-bond formation energy (-1 kJ). At low temperature close to 400 K, a morphological ring-linear transition is also observed which is explained by the decrease of H bonds in linear aggregates and the increase of H bonds in rings with decreasing T. This transition temperature T_r^* is defined by the position of a maximum peak of $\delta_{n_{hb,r}}$. As expected from the simulation snapshots, energetically favored but entropically unfavored ring aggregates dominate at low temperature, but H bonds in rings start to be broken leading to linear aggregates at $T = T_r^*$. Here, T_r^* again depends on the criterion for H-bond formation, -1 kJ because of its definition. However, in our previous work [45] done for a single SMP precursor, we found that the nonbonded energy distribution at the ring opening transition temperature is bimodal and two configurations emerge at around -60 kJ and at above 0 kJ. Therefore, T_r^* is not sensitive to the choice of the value of the criterion if the value is less than 0 kJ. T_r^*'s for different values of the criterion calculated for the $M = 4$ system as shown in Table S1 in the Supplementary Material [57] also support the validity of the argument. The ring-linear transition at a certain density at a given temperature has been reported in previous studies, but the morphological behavior as a function of temperature was only predicted from mean-field theory [36–38]. To our knowledge, there has not been an explicit observation of the ring-linear transition temperature at a given density by numerical simulation so far. As the temperature increases further to $T = T_l^*$, a condensation-evaporation transition occurs by H-bond breaking.

The probability distribution of the aggregate sizes shown in Fig. 7 helps to understand the thermodynamics of the transitions defined above. At $T = T_r^* = 392$ K, a ring of size s starts to convert into a linear aggregate of size s. Due to the interplay between energy gain from H bonds and energetic penalty by chain stiffness, a single-membered ring is hardly

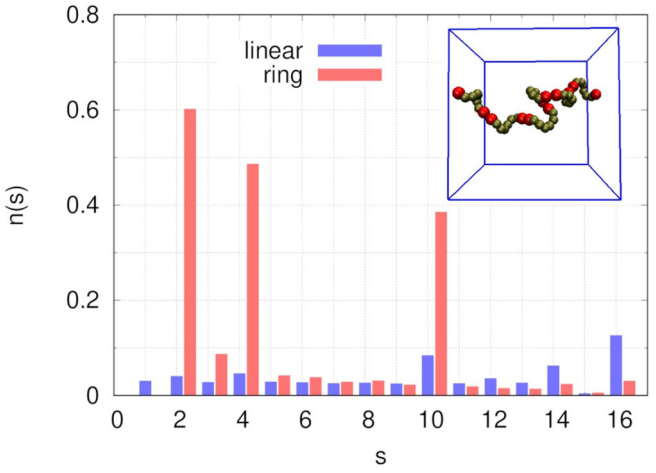

FIG. 7. Average number of s-membered linear (left column at each s) and ring aggregates (right column at each s) at $T = T_r^* = 392$ K for a $M = 16$ PEG system.

observed and a two-membered ring is most probable. Even larger rings are less probable due to the entropic penalty of loop formation. Our previous work found that a ring opening transition temperature of a single PEG of the same model varies nonmonotonously as the degree of polymerization and shows a maximum at around $N = 16$, which has the same number of monomers as the $s = 2$ ring aggregate [45]. Therefore, absence of one-membered rings and the nonmonotonous size distribution in this work are well consistent with our previous work. However, over the whole range of aggregate sizes, odd-membered rings are rare because we have a finite number of precursors in a system, which restricts the size of aggregates. For example, in the system involving 16 precursors, since a one-membered ring is strongly forbidden and the total number of polymers is even, odd-membered rings are missing. It is also interesting to note that a 10-membered ring is pronounced at this temperature which is, however, caused by a finite-size effect. As one can see in the inset of Fig. 7, a periodic boundary condition allows the aggregates to percolate the simulation box, which is defined as a percolating ring. This percolating ring has the same topology of no chain end with an actual ring which does not cross over the boundary in Fig. 4(a) called a nonpercolating ring. A percolating ring has the same number of H bonds with a nonpercolating ring of the same size, so it leads to overestimation of the $g(U)$, which possibly overestimates T_r^* as well. The finite-size effect on T_r^* will be discussed shortly. At $T = T_l^* = 560$ K as shown in Fig. S3 in the Supplementary Material [57], the distribution of linear aggregates decays exponentially which was proven in many previous studies [29–32]. For the ring aggregates, the one-membered ring is still missing and the two-membered ring is highly probable. But overall, it also seems to follow an exponential distribution.

As mentioned above, a finite-size effect exists especially affecting the ring-linear transition temperature. Figure 8(a) shows canonical specific heats for the systems of $\phi = 0.065$ for different system size. The system of $L = 6.00$ nm was used in the other analyses. We find that the shape of $C_v(T)$ for the $L = 8.01$-nm system is almost the same as for the

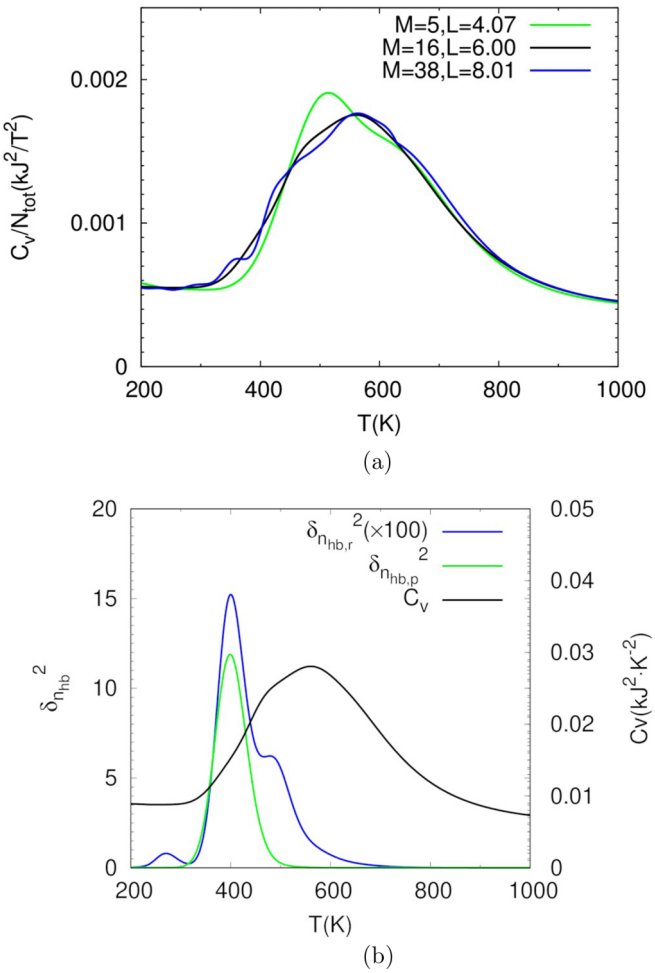

FIG. 8. (a) Canonical specific heats for the systems of volume fraction, $\phi = 0.065$ for different system sizes, $L = 4.07$ (green, light gray), 6.00 (black), and 8.01 nm (blue, gray). (b) Fluctuations of the number of H bonds for nonpercolating ring (blue, gray) and percolating ring (green, light gray) as well as the specific heat (black) on the right axis as a function of temperature for $L = 6.00$ nm.

original system. However, the small system of $L = 4.07$ nm looks different from the others regarding the position of the peaks as well as the overall shape. We found that the large peak at $T \approx 520$ K is caused by the highly overestimated T_r^*. As shown in Fig. 7, the two-membered ring is most probable at low temperature. The two-membered linear aggregate has a contour length of 5.29 nm (2.395 nm for each precursor and 0.5 nm for the H bond) which is larger than the box size of the small system. Therefore, the number of states of percolating rings significantly increases resulting in overestimation of $g(U)$ and T_r^*. Therefore, we should use system sizes larger than at least a contour length of the two-membered ring to avoid the critical finite-size effect.

As mentioned above, the average energies of percolating and nonpercolating rings are comparable unless the fraction of one-membered rings against the energetic penalty of chain stiffness is significant. The entropic penalties for the two morphologies, however, come from different origins. For the nonpercolating ring, the entropic penalty mainly originates from the loop formation, but for the percolating one it

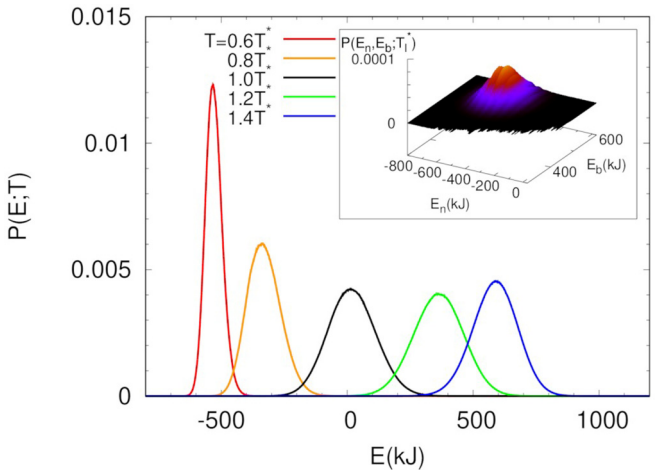

FIG. 9. Probability distribution of energies at different temperatures (from left to right as increasing T) for a $M = 16$ PEG system. Here the black curve is the one at the transition temperature. The inset shows the two-dimensional probability distribution of configurations as a function of nonbonded (E_n) and bonded energies (E_b).

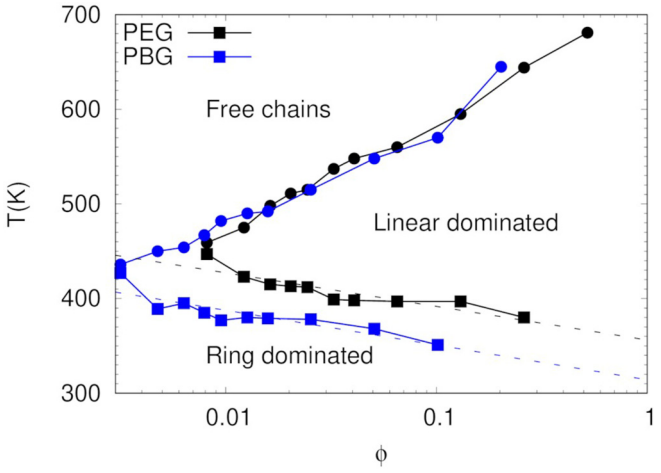

FIG. 10. T-ϕ phase diagram for self-complementary SMP systems of PEG (black) and PBG (blue, gray) spacers. Density is normalized to volume fraction of monomers, ϕ. Circles represent the linear-free chain transition temperature and squares represent the ring-linear transition. Dashed lines indicate the fitted functions of the ring-linear transition temperatures with $T_r^* = b_1 - b_2 \ln(\phi)$, where b_1 and b_2 are fitting parameters.

originates from the probability of finding another sticker in space, which depends on the sticker density. Due to the different entropic costs for the morphology formation, the transition temperatures could have been different, but the number fluctuation of the H bonds in rings in Fig. 6, shows only one peak. To understand this behavior, we calculate the number fluctuations of H bonds in nonpercolating (blue) and percolating rings (red) in the $M = 16$, $L = 6$-nm PEG system as shown in Fig. 8(b). In this figure, the positions of the peaks for the two morphologies are almost the same, which indicates that the effect of percolating rings on T_r^* is not significant. Even if the origins of the entropic penalty of forming two morphologies are different, they are leading to almost the same T_r^*. Therefore, we believe that the transition temperatures obtained in our systems are not affected significantly by the small system size.

One of the great advantages of the SAMC sampling method is the possibility of investigating thermodynamic properties of the system close to the transition point. Here we study the nature of the phase transition in the SMP system. From the canonical specific heat in Fig. 6, we can find one thermodynamic transition, a linear-free chain transition. This transition has no signature of a first-order transition from the microcanonical specific heat in Fig. 3, i.e., negative microcanonical specific heat. We also plot the probability distribution of energies at different temperatures in Fig. 9 using the relation $P(E) = g(E)\exp(-E/k_BT)/Z$, where Z is canonical partition function. In this figure, we can see a unimodal distribution at $T = T_l^*$ which indicates a continuous transition. Our previous work done on a single SMP precursor has shown that two morphologies can coexist at the transition temperature for a continuous ring-opening transition of very long SMP precursors [45]. Such a behavior can be identified by the two-dimensional (2D) DOS as a function of nonbonded and bonded energies as shown in the inset of Fig. 9 which is constructed from the 2D DOS. In this figure, no distinct coexistence peaks are observed. A bumpy surface on the broad distribution is weakly visible caused by the finite number of precursors in the system, which is expected to disappear in the thermodynamic limit. Therefore, we can conclude that this transition is a continuous transition without coexistence of different configurational energies.

Moving our attention to the density dependence of the system, we calculate $C_v(T)$ for systems of different densities as shown in Fig. S4 in the Supplementary Material [57]. Here the specific heat is normalized by the number of particles in the system. In this figure, the position of the main peak in C_v, defined as T_l^*, increases with increasing density. Using the obtained transition temperatures for the different densities in Figs. 6 and S4, we draw a T-ϕ phase diagram of SMPs in Fig. 10. Two different spacer systems, PEG and PBG, are plotted together and ϕ is the volume fraction of the PEG and PBG monomers, respectively. As explained above, there are a morphological transition between ring- and linear-dominated morphologies at low temperature and a thermodynamic transition corresponding to the condensation-evaporation of chains. The two transition temperatures vary in opposite ways with increasing ϕ. Unfortunately, the transition temperatures can not be interpreted by classical polymerization theories [29–32,36], because the theories used chemical equilibrium constants at a given temperature, which are, however, temperature dependent. Nevertheless, a tendency of the transition temperature observed in this work can be qualitatively understood by the following argument.

We first assume morphological coexistence at the transition temperatures. Although the transitions involved in this study have no coexistence of different configurational energies, there can be the morphological coexistence at the transition temperatures, because we defined the H bond as a binary and it determines the morphology of aggregates. Under this assumption, we can now consider the Helmholtz free energy $\Delta\bar{F} = \Delta\bar{E} - T\Delta\bar{S}$, where $\bar{E}$ and $\bar{S}$ are the mean energy and entropy

density per precursor, respectively. The transition temperature is determined by $\Delta\bar{F} = 0$, and $T^* = \Delta\bar{E}/\Delta\bar{S}$. Here Δ is defined as a value of a function at a high-temperature state minus that at a low-temperature state, for example, $\Delta\bar{E} = \bar{E}(\text{free-chains}) - \bar{E}(\text{linear-dominated})$ at $T = T_l^*$. Assuming that chain conformational energies of two states are almost the same, we expect $\Delta\bar{E} \approx \Delta\bar{E}_{hb}$ which is positive and is almost constant independent of ϕ for both transitions. An entropy change is mainly composed of three contributions, translational entropy $\Delta\bar{S}_{tr}$, polymer conformational entropy $\Delta\bar{S}_p$, and H-bond forming entropy $\Delta\bar{S}_{hb}$. The H-bond forming entropy can be approximated by $\Delta\bar{S}_{hb} \sim -k_B \ln P_{hb}/2$, where P_{hb} is a probability of two stickers forming a hydrogen bond. Here the only contribution strongly varying with the precursor density is $\Delta\bar{S}_{hb}$ for both transitions. For the linear-free chain transition P_{hb} is proportional to $v_{hb}\rho_{st}$, where v_{hb} is an effective volume of H-bond forming between two stickers and ρ_{st} is the number of stickers in a unit volume. Since v_{hb} is fixed for a given sticker force field, P_{hb} increases with increasing ϕ resulting in decreasing $\Delta\bar{S}_{hb}$ and $\Delta\bar{S}$. Therefore, T_l^* increases as ϕ increases.

For the ring-linear transition temperature, let us assume that one of the H bonds in a ring aggregate of the average size $\langle s\rangle$ at $T = T_r^*$ is broken and the ring converts into a linear aggregate. In this case, $P_{hb} \sim v_{hb}/R_{ee}(\langle s\rangle)^3$, where $R_{ee}(\langle s\rangle)$ is the end-to-end distance of a linear aggregate of size $\langle s\rangle$. As ϕ of the system increases, $\langle s\rangle$ also increases which results in increasing $R_{ee}(\langle s\rangle)$ for self-avoiding walks. Therefore, $\Delta\bar{S}$ decreases with increasing ϕ which leads to the negative slope of T_r^*. This behavior is also well consistent with the previous work which provided a qualitative description of ring-linear transition temperature as a function of the ratio of association strength to temperature [36].

Comparing PEG and PBG spacer systems, T_l^* for the two systems is almost the same but T_r^* for PEG is higher than for PBG at the same ϕ. The fact that the T_l^* are almost the same can be understood by the argument of $\Delta\bar{S}$ which is again depending on P_{hb}. At the same monomer volume fraction the sticker number densities are also the same for the two cases, resulting in the same T_l^*. For T_r^*, P_{hb} of the two systems should be compared, which mainly depends on the average size of the linear aggregates at the transition temperature. Because the spatial dimension of the PBG aggregates is larger than of PEG aggregates due to the larger size of the PBG precursor, the entropic penalty to form PBG ring aggregates is larger. Therefore, the PEG ring is entropically more stable than the PBG ring, which leads to the higher T_r^* of PEG.

The phase diagram as a function of of mass density, ρ_m, in Fig. S5 in the Supplementary Material [57] helps to compare our results to experimental data. Here T_r^* decreases linearly with $\ln\rho_m$, so we could fit T_r^* with the function, $T_r^* = c_1 - c_2 \ln\rho_m$, where c_1 and c_2 are fitting parameters. This extrapolation allows to roughly estimate morphologies of meltlike SMPs at room temperature, $T = 300$ K, in such a way that both PEG and PBG SMP melts whose mass density are close to 1 g/cm^3 have a ring-linear transition temperature similar to 300 K. Because the ring-linear transition is a continuous morphological transition, the systems are expected to be a ring-linear mixture at room temperature. Because a PBG bead is heavier PBG than a PEG bead, the transition temperatures

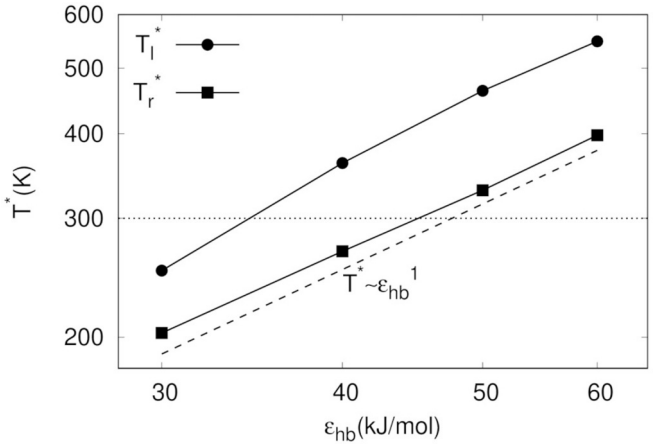

FIG. 11. Log-log plot of T_l^* (circle) and T_r^* (square) for a $M = 10$ PEG system at $\phi = 0.040$ as a function of ϵ_{hb}. A dashed line represents a scaling of $T^* \sim \epsilon_{hb}^1$, and a dotted line represents $T = 300$ K.

of the PBG system are lower than those of the PEG system at the same ρ_m. The same result is obtained also in Fig. 10 for SMPs of the volume fraction close to unity.

However, the actual association strength of the H bond in solution, which is still hard to determine in experiments but is set to $\epsilon_{hb} = 60$ kJ/mol in Eq. (1) in this work, strongly affects the transition temperature. Therefore, we calculated the transition temperature as a function of ϵ_{hb} as shown in Fig. 11. In this figure, both transition temperatures increase proportionally to ϵ_{hb}^1, which also supports our assumption $\Delta\bar{E} \approx \Delta\bar{E}_{hb}$. We can also find the range of ϵ_{hb} resulting in different morphologies at a given temperature. For example, the PEG system of $\phi = 0.040$ ($\rho_m = 0.0203$ g/cm^3) at $T = 300$ K has free chain–, linear-, and ring-dominated morphologies when $\epsilon_{hb} < 34.7$ kJ/mol, 34.7 kJ/mol $< \epsilon_{hb} <$ 45.0 kJ/mol, and $\epsilon_{hb} > 45.0$ kJ/mol, respectively. Therefore, the linear scaling of the transition temperature by the association energy not only allows to estimate the morphological transition temperatures for different associating motifs but also opens a possibility of synthesizing new materials whose morphology and rheology are thermodynamically controlled.

IV. CONCLUSIONS

In this paper, equilibrium morphology and phase behavior of H-bonding SMPs built on PEG and PBG were investigated in a wide range of temperature and density using RESAMC simulation. Most importantly, we found two morphological transitions, a ring-linear and a linear-free chain transitions. It turned out that the latter is a thermodynamic transition which is continuous without coexistence of configurational energies as occurred for a single precursor chain. Through a finite-size analysis, we found that percolating rings due to the periodic boundary condition do not significantly influence the ring-linear transition temperature of the investigated system size. At room temperature and in the semidilute regime, our simulation shows ring-dominated morphology both for PEG and for PBG. Extrapolation of the ring-linear transition temperature allowed a rough estimation of morphology of SMP

melts, which turned out to be a ring-linear mixture. We also analyzed a relation between H-bonding interaction strength and the transition temperatures, which helps to understand how the choice of the sticker molecule affects the morphology of SMPs.

As a future work, the dynamic and rheological behavior of SMPs including ring morphology should be addressed further. It is expected that topological effects of a ring such as a threading leads to slower dynamics than expected, which was shown in inherent ring polymer systems. Moreover, concatenated and knotted rings can be formed due to the reversible H bonds. Of course, the topology is not fixed for the system due to the reversible H bonds, so the topological relaxation time may compete with the H-bond lifetime, which determines a characteristic relaxation time of the system. Therefore, it is worthwhile to investigate the dynamic behavior of the model H-bonding SMPs focusing on the ring morphology.

ACKNOWLEDGMENTS

We thank Dr. A. Brás for discussions on experiments of supramolecular polymers. We also thank Dr. T. Shakirov for valuable advices on the SAMC method. We acknowledge the financial support from the German Research Foundation (Grant No. PA 473/14-1) and computing time on the IANVS cluster at Martin-Luther University Halle-Wittenberg.

[1] M. A. Winnik and A. Yekta, Associative polymers in aqueous solution, Curr. Opin. Collid Interface Sci. **2**, 424 (1997).

[2] L. Brunsveld, B. Folmer, E. W. Meijer, and R. Sijbesma, Supramolecular polymers, Chem. Rev. **101**, 4071 (2001).

[3] R. P. Wool, Self-healing materials: A review, Soft Matter **4**, 400 (2008).

[4] J. D. Fox and S. J. Rowan, Supramolecular polymerizations and main-chain supramolecular polymers, Macromolecules **42**, 6823 (2009).

[5] C. Chassenieux, T. Nicolai, and L. Benyahia, Rheology of associative polymer solutions, Curr. Opin. Collid Interface Sci. **16**, 18 (2011).

[6] T. Aida, E. Meijer, and S. Stupp, Functional supramolecular polymers, Science **335**, 813 (2012).

[7] F. Herbst, D. Döhler, P. Michael, and W. H. Binder, Self-healing polymers via supramolecular forces, Macromol. Rapid Commun. **34**, 203 (2013).

[8] W. H. Binder, *Self-healing Polymers: From Principles to Applications* (John Wiley & Sons, New York, 2013).

[9] R. F. Lange, M. Van Gurp, and E. Meijer, Hydrogen-bonded supramolecular polymer networks, J. Polym. Sci. A **37**, 3657 (1999).

[10] W. H. Binder and R. Zirbs, Supramolecular polymers and networkswith hydrogen bonds in the main-and side-chain, *Hydrogen Bonded Polymers* (Springer, Berlin, 2006), pp. 1–78.

[11] W. H. Binder, L. Bouteiller, G. ten Brinke, O. Ikkala, V. Rotello, J. Ruokolainen, S. Srivastava, H. Xu, and R. Zirbs, *Hydrogen Bonded Polymers* (Springer, Berlin, 2007), Vol. 207.

[12] S. Chen, D. Döhler, and W. H. Binder, Rheology of hydrogen-bonded dendritic supramolecular polymer networks in the melt state, Polymer **107**, 466 (2016).

[13] F. H. Beijer, R. P. Sijbesma, H. Kooijman, A. L. Spek, and E. Meijer, Strong dimerization of ureidopyrimidones via quadruple hydrogen bonding, J. Am. Chem. Soc. **120**, 6761 (1998).

[14] B. J. Folmer, R. Sijbesma, R. Versteegen, J. Van der Rijt, and E. Meijer, Supramolecular polymer materials: Chain extension of telechelic polymers using a reactive hydrogen-bonding synthon, Adv. Mater. **12**, 874 (2000).

[15] H. Kautz, D. Van Beek, R. P. Sijbesma, and E. Meijer, Cooperative end-to-end and lateral hydrogen-bonding motifs in supramolecular thermoplastic elastomers, Macromolecules **39**, 4265 (2006).

[16] A. R. Brás, C. H. Hövelmann, W. Antonius, J. Teixeira, A. Radulescu, J. Allgaier, W. Pyckhout-Hintzen, A. Wischnewski, and D. Richter, Molecular approach to supramolecular polymer assembly by small angle neutron scattering, Macromolecules **46**, 9446 (2013).

[17] M. Krutyeva, A. Brás, W. Antonius, C. Hövelmann, A. Poulos, J. Allgaier, A. Radulescu, P. Lindner, W. Pyckhout-Hintzen, A. Wischnewski *et al.*, Association behavior, diffusion, and viscosity of end-functionalized supramolecular poly (ethylene glycol) in the melt state, Macromolecules **48**, 8933 (2015).

[18] M. Monkenbusch, M. Krutyeva, W. Pyckhout-Hintzen, W. Antonius, C. H. Hövelmann, J. Allgaier, A. Brás, B. Farago, A. Wischnewski, and D. Richter, Molecular View on Supramolecular Chain and Association Dynamics, Phys. Rev. Lett. **117**, 147802 (2016).

[19] J. Sprakel, E. Spruijt, M. C. Stuart, N. Besseling, M. Lettinga, and J. van der Gucht, Shear banding and rheochaos in associative polymer networks, Soft Matter **4**, 1696 (2008).

[20] K. Tam, R. Jenkins, M. Winnik, and D. Bassett, A structural model of hydrophobically modified urethane- ethoxylate (heur) associative polymers in shear flows, Macromolecules **31**, 4149 (1998).

[21] D. Montarnal, N. Delbosc, C. Chamignon, M.-A. Virolleaud, Y. Luo, C. J. Hawker, E. Drockenmuller, and J. Bernard, Highly ordered nanoporous films from supramolecular diblock copolymers with hydrogen-bonding junctions, Angew. Chem. **54**, 11117 (2015).

[22] J. Roosma, T. Mes, P. Leclère, A. R. Palmans, and E. Meijer, Supramolecular materials from benzene-1, 3, 5-tricarboxamide-based nanorods, J. Am. Chem. Soc. **130**, 1120 (2008).

[23] M. Rubinstein and A. V. Dobrynin, Associations leading to formation of reversible networks and gels, Curr. Opin. Collid Interface Sci. **4**, 83 (1999).

[24] A. R. Brás, Molecular self-assembly and dynamics on supramolecular polymers (unpublished).

[25] J. D. Halverson, G. S. Grest, A. Y. Grosberg, and K. Kremer, Rheology of Ring Polymer Melts: From Linear Contaminants to Ring-Linear Blends, Phys. Rev. Lett. **108**, 038301 (2012).

[26] E. Lee, S. Kim, and Y. Jung, Slowing down of ring polymer diffusion caused by inter-ring threading, Macromol. Rapid Commun. **36**, 1115 (2015).

[27] E. Lee and Y. Jung, Slow dynamics of ring polymer melts by asymmetric interaction of threading configuration: Monte Carlo study of a dynamically constrained lattice model, Polymers **11**, 516 (2019).

[28] M. L. Mansfield and J. F. Douglas, Properties of knotted ring polymers. ii. Transport properties, J. Chem. Phys. **133**, 044904 (2010).
[29] H. Jacobson and W. H. Stockmayer, Intramolecular reaction in polycondensations. i. The theory of linear systems, J. Chem. Phys. **18**, 1600 (1950).
[30] P. Flory, U. Suter, and M. Mutter, Macrocyclization equilibriums. 1. Theory, J. Am. Chem. Soc. **98**, 5733 (1976).
[31] S. Kuchanov, H. Slot, and A. Stroeks, Development of a quantitative theory of polycondensation, Prog. Polym. Sci. **29**, 563 (2004).
[32] G. Ercolani, L. Mandolini, P. Mencarelli, and S. Roelens, Macrocyclization under thermodynamic control. A theoretical study and its application to the equilibrium cyclooligomerization of. beta.-propiolactone, J. Am. Chem. Soc. **115**, 3901 (1993).
[33] A. Milchev and D. P. Landau, Monte Carlo study of semiflexible living polymers, Phys. Rev. E **52**, 6431 (1995).
[34] J. Dudowicz, K. F. Freed, and J. F. Douglas, Lattice model of living polymerization. i. Basic thermodynamic properties, J. Chem. Phys. **111**, 7116 (1999).
[35] A. Milchev, J. P. Wittmer, and D. P. Landau, Dynamical Monte Carlo study of equilibrium polymers: Effects of high density and ring formation, Phys. Rev. E **61**, 2959 (2000).
[36] C.-C. Chen and E. E. Dormidontova, Supramolecular polymer formation by metal-ligand complexation: Monte Carlo simulations and analytical modeling, J. Am. Chem. Soc. **126**, 14972 (2004).
[37] M. C. Hagy, C.-C. Chen, and E. E. Dormidontova, Effect of orientational specificity of complexation on the behavior of supramolecular polymers: Theory and simulation, Macromolecules **40**, 3408 (2007).
[38] Z. Li, H. Djohari, and E. E. Dormidontova, Molecular dynamics simulations of supramolecular polymer rheology, J. Chem. Phys. **133**, 184904 (2010).
[39] E. B. Stukalin, L.-H. Cai, N. A. Kumar, L. Leibler, and M. Rubinstein, Self-healing of unentangled polymer networks with reversible bonds, Macromolecules **46**, 7525 (2013).
[40] D. Amin, A. E. Likhtman, and Z. Wang, Dynamics in supramolecular polymer networks formed by associating telechelic chains, Macromolecules **49**, 7510 (2016).
[41] T. Furuya and T. Koga, Molecular simulation of structure formation and rheological properties of mixtures of telechelic and monofunctional associating polymer, Polym. Phys. **56**, 1251 (2018).
[42] R. D. Groot and W. G. Agterof, Monte Carlo study of associative polymer networks. i. Equation of state, J. Chem. Phys. **100**, 1649 (1994).
[43] S. K. Kumar and J. F. Douglas, Gelation in Physically Associating Polymer Solutions, Phys. Rev. Lett. **87**, 188301 (2001).
[44] F. Tanaka, Intramolecular micelles and intermolecular crosslinks in thermoreversible gels of associating polymers, J. Non-Cryst. Solids **307**, 688 (2002).
[45] E. Lee and W. Paul, Thermodynamics of single polyethylene and polybutylene glycols with hydrogen-bonding ends: A transition from looped to open conformations, J. Chem. Phys. **148**, 084905 (2018).
[46] C. L. Dias, T. Ala-Nissila, M. Grant, and M. Karttunen, Three-dimensional "mercedes-benz" model for water, J. Chem. Phys **131**, 054505 (2009).
[47] J. Emsley, Very strong hydrogen bonding, Chem. Soc. Rev. **9**, 91 (1980).
[48] F. Liang, A theory on flat histogram Monte Carlo algorithms, J. Stat. Phys. **122**, 511 (2006).
[49] F. Liang, C. Liu, and R. J. Carroll, Stochastic approximation in Monte Carlo computation, J. Am. Stat. Assoc. **102**, 305 (2007).
[50] Z. Wang, L. Wang, and X. He, Phase transition of a single protein-like copolymer chain, Soft Matter **9**, 3106 (2013).
[51] Z. Wang, L. Wang, Y. Chen, and X. He, Phase transition behaviours of a single dendritic polymer, Soft Matter **10**, 4142 (2014).
[52] W. Janke and W. Paul, Thermodynamics and structure of macromolecules from flat-histogram Monte Carlo simulations, Soft Matter **12**, 642 (2016).
[53] T. Vogel, Y. W. Li, T. Wüst, and D. P. Landau, Generic, Hierarchical Framework for Massively Parallel Wang-Landau Sampling, Phys. Rev. Lett. **110**, 210603 (2013).
[54] T. Vogel, Y. W. Li, T. Wüst, and D. P. Landau, Scalable replica-exchange framework for Wang-Landau sampling, Phys. Rev. E **90**, 023302 (2014).
[55] R. H. Swendsen and J.-S. Wang, Replica Monte Carlo Simulation of Spin-Glasses, Phys. Rev. Lett. **57**, 2607 (1986).
[56] T. Shakirov, S. Zablotskiy, A. Böker, V. Ivanov, and W. Paul, Comparison of Boltzmann and Gibbs entropies for the analysis of single-chain phase transitions, Eur. Phys. J. Spec. Top. **226**, 705 (2017).
[57] See Supplemental Material at http://link.aps.org/supplemental/10.1103/PhysRevE.100.012502 for more results which are supportive of our analysis.